Shallow magma storage beneath Mt. Etna: Evidence from new attenuation tomography and existing velocity models

I. Castro-Melgar[1], J. Prudencio[1,2], E. Del Pezzo[2,3], E. Giampiccolo[4], and J. M. Ibáñez[1,2,3]

[1] Department of Theoretical Physics and Cosmos, University of Granada, Granada, Spain.

[2] Andalusian Institute of Geophysics, University of Granada, Granada, Spain.

[3] Istituto Nazionale di Geofisica e Vulcanologia, Osservatorio Vesuviano, Napoli, Italy.

[4] Istituto Nazionale di Geofisica e Vulcanologia, Osservatorio Etneo, Catania, Italy.

Corresponding author: Janire Prudencio (janire@ugr.es)

Key Points:

- List up to three key points (at least one is required)
- Key Points summarize the main points and conclusions of the article
- Each must be 140 characters or less with no special characters or acronyms.

Abstract

We present a new three-dimensional (3D) image of attenuation beneath Mt. Etna volcano based on the coda normalization method. Mt. Etna is an ideal natural laboratory for the application of new or unconventional tomography techniques owing to high levels of seismicity spanning a wide range of epicentral distances and depths. We retrieved seismic waveforms from the database generated in the 2014 TOMO-ETNA seismic experiment and performed a joint interpretation of tomographic and geophysical inversion models to better constrain interpretations of the volcanic structure. We compared the attenuation tomography results with seismic inversion models (two P wave seismic models and a 3D coda wave seismic attenuation model) and the literature to highlight and interpret structural elements and their impact on the volcano dynamics. We created a new image of the inner structure of Mt. Etna that will help to constrain present and future volcanic behavior. In particular, we focused on magma storage below the summit area and identified a large high-attenuation volume that is characterized by physical properties compatible with the presence of magma and other fluids. The existence of such a large volume of magma in the shallow crust below Mt. Etna has implications for the eruptive potential of the volcano.

1 Introduction

Determining the location and size of potential magma reservoirs is crucial to constraining the size of future eruptions or eruptive frequency. Magma accumulation and melt migration have been the focus of extensive research at Mt. Etna volcano. Recent geophysical imaging of Mt. Etna has shown the growing importance of several geological bodies in explaining the migration of eruptive materials inside the volcano. One such body, known as the High Velocity Body (HVB), is a highly consolidated structure located below the central-southern part of the volcano. The HVB has been observed in several tomography studies (Giampiccolo et al., 2020 and references therein) and is interpreted as a massive accumulation of intrusions within the sedimentary basement. In addition, new structural elements have been identified tomographically to the west and southwest of the main volcanic edifice (e.g., Díaz-Moreno et al. 2018 and references therein). Despite not being widely discussed and interpreted in studies based on travel time tomography, these bodies have been well resolved using other techniques. In addition, recent studies (Alparone et al., 2015; Barberi et al., 2016) have found a strong association between deep seismicity beneath Mt. Etna and these geological objects, indicating the need for further study. Apparent contradictions between older and newer tomographic images possibly reflect the increased sensitivity of new tomography techniques to rock heterogeneity associated with the presence of dykes and fractures permeated by volcanic fluids. Moreover, volcanoes are dynamic systems, where fluid movements accompany the temporal evolution of the structural

elements that comprise the bulk of the volcano; this is reflected in variation between tomographic images. Detecting these changes is crucial for improving early-warning protocols.

From a geological perspective, time dependent tomography models—4D models—allow us to study the temporal evolution of volcanic structures and the fluids within them in order to understand the pre-eruptive behavior of the system. Passive 4D tomographic models of active volcanoes (e.g., De Gori et al., 2011; Giampiccolo et al., 2020; Koulakov et al., 2018; Koulakov and Vargas, 2018; Patanè et al., 2006) rely on strict hypotheses for seismic datasets; for example, assuming the same source-station configuration for different time periods, which is uncommon. They are also affected by large uncertainties; for example, uncertainties in source locations for different time periods. An alternative approach is to perform active seismic experiments, which provide an instantaneous snapshot of the volcanic system (e.g., BenZvi et al., 2009; García-Yeguas et al., 2012; Ibáñez et al., 2008, 2016; Shalev et al., 2010; Voight et al., 2014; Zandomeneghi et al., 2009). There are obvious limitations to this procedure, including the logistical complexity, high economic cost, and resolution limits associated with the distribution of the active seismic sources. However, once these data are available, new methodologies that allow modelling and inverting for different seismic attributes can better inform on the structure and dynamics of the volcanic system (Prudencio et al. 2013a, 2013b, 2015a, 2015b).

Mt. Etna is an ideal natural laboratory for the application of new or unconventional tomography techniques owing to high levels of seismicity spanning a wide range of epicentral distances and depths, and because of the extended network of its monitoring institution (the Istituto Nazionale di Geofisica e Vulcanologia, Osservatorio Etneo, INGV-OE). It is therefore unsurprising that so many tomographic works have used Mt. Etna as a template for exporting

new methodologies to other volcanoes. Geographical, morphological, geological, volcanological, and geophysical descriptions of Mt. Etna volcano are widely available in the literature, and highlight the importance of this volcanic system (e.g., Aloisi et al., 2020; Azzaro et al., 2012; Barreca et al., 2018, 2020; Branca and Ferrara, 2013; De Guidi et al., 2015; Neri et al., 2009; Presti et al., 2020); studies focused on geophysical and tomographic models of the volcano are also abundant (i.e., Chiarabba et al., 2004; Bonforte et al., 2008; De Gori et al., 2011; Diaz-Moreno et al., 2018; Giampiccolo et al., 2020; Guardo and De Siena, 2017; Guardo et al., 2020; Ibáñez et al., 2020; Laiolo et al., 2019; Martínez-Arévalo et al., 2005; Patanè et al., 2002.

In this work, we present a new three-dimensional (3D) image of Mt. Etna volcano based on seismic attenuation techniques. The coda normalization method (Aki, 1980; Del Pezzo et al. 2006; De Siena et al. 2014a, 2014b; Prudencio et al. 2015a, 2015b; Prudencio & Manga, 2020), was used for the first time in this setting to study P wave attenuation. We retrieved seismic waveforms from the database generated in the 2014 TOMO-ETNA seismic experiment (Ibáñez et al. 2016a, 2016b). The travel-time and coda-wave measurements from this dataset have been used to perform direct P wave velocity tomography (Diaz-Moreno et al., 2018), and to separate the effects of intrinsic and scattering attenuation (Ibáñez et al., 2020), among others. This database corresponds to an active seismic experiment using air guns and a large number of temporary and permanent seismic stations. The high number of receiver-source couples available provides homogeneous spatial coverage that increases the quality of the obtained images. These images were generated over a short time interval and reflect a snapshot of the structure of Mt. Etna at the time of their realization. During the investigated period, Mt. Etna was characterized

by several episodes of Strombolian activity and lava emissions from the main upper craters (i.e., Viccaro et al. 2016 and references therein).

Volcanoes are complex structures that respond differently to different geodynamic conditions. This complexity is reflected in the difficulty of interpreting structures from single geophysical observations and/or tomographic models. Joint interpretation of tomographic and geophysical models can better constrain interpretations of a volcanic structure. In recent works (e.g., Basant et al., 2021; De Siena et al. 2017; Cordell et al., 2020; García-Yeguas et al., 2017), the integration of different geophysical models has highlighted important structures for different volcanic scenarios. Here, we compared our attenuation tomography results with geophysical models—two P wave seismic tomographies (Díaz-Moreno et al., 2018; Giampiccolo et al., 2020) and a 3D coda waves seismic attenuation model (Giampiccolo et al., 2021)—and the literature to highlight and interpret structural elements and their role in volcano dynamics at Mt. Etna. In particular, we focused on magma storage below the summit, where high-attenuation volumes mark the presence of an extended molten body. This body is the likely cause of the continuous volcanic activity, including the highly energetic eruption underway at the time of writing (March 2021).

2 Methods and Seismic Data

2.1 Coda normalization method

Coda normalization (CN) was based on the approach developed Del Pezzo et al. (2006); this method provides a measure of the single-path attenuation coefficient using the phenomenological coda wave properties. Aki (1980) first proposed this method to calculate

space-averaged S wave attenuation in Japan. By normalizing the direct S wave spectrum and using a late "lapse time" (tc, the time spanned from the origin time along the coda), it was demonstrated that the source intensity, the site transfer functions, and the instrument transfer functions disappear in the ratio. The method is applied to obtain single station estimates of the total inverse P wave quality factor (Q) along the seismic path. Here, we briefly review the method; for more detailed descriptions, please see Del Pezzo et al (2006), De Siena et al. (2014a, 2014b), and/or Prudencio et al. (2015a, 2015b).

The average total attenuation coefficient, QT-1, measures the average loss suffered by seismic energy body waves owing to heterogeneous attenuation (and thus excluding geometrical spreading). In the spectral domain and for a single source (i)–station (j) observation:

$$E_{ij}(f,r) = S_i(f)\theta_{ij}(\vartheta,\phi)I_j(f)T_j(f)G_{ij}(r)x\ exp\left(-2\pi f\frac{t_{ij}(r)}{Q_T^{ij}(r)}\right) \qquad (1)$$

in which E(f,r) is the energy density spectrum, where f is the frequency of the S wave radiation emitted by source i at distance r along the source-station ray-path; Si(f) is the source energy spectrum, modulated by the radiation pattern $\theta(\upsilon,\phi)$; Ij is the instrument transfer function; Tj is the site transfer function; G is the geometrical spreading; tij is the travel time along the ray; and QTij is the total quality factor calculated along the ray-path, which defines the fractional energy lost per cycle (ΔE) according to the equation $QTij = -2\pi Eij/\Delta Eij$. To avoid the effects of diffraction, waveguides, and surface waves in given frequency bands, G and QT-1 are preliminarily inverted and then kept constant, inverting only for spatial variations of quality factors (De Siena et al., 2014a).

Yoshimoto et al. (1993) proved that the CN method can be applied to measure average P wave attenuation (P wave quality factor, Qp) by using the S wave coda to normalize observations, and remove source, site, and instrumental effects.

In this study, we used active sources that only produce P waves; as such, we could neglect radiation pattern effects. Ibáñez et al. (2020) showed that pure compressional signals convert to shear after a few mean free paths from the signal origin. However, the first arrivals remain purely compressional (Díaz-Moreno et al., 2016, 2018; García et al., 2016). Using a 1 s window guarantied that we obtained pure direct P waves.

The seismic attenuation coefficient at each node of the inversion grid (Qb) was obtained using the following equation (Del Pezzo et al., 2006):

$$R_{ij} = K(f) - \pi f \sum_{b=1}^{B} l_{ijb} s_b Q_b^{-1}, \qquad (2)$$

where R_{ij} is the spectral ratio between the direct P wave energy (E_{ij}^{P}) and the coda energy at a given lapse (E_{ij}^{C} *(fc, tc)*), pre-multiplied by r; index *b* indicates the *b*th block and B represents the total number of blocks; s_b represents the slowness*;* l_{ijb} is the length of the ray-segment crossing the *b*th block for each *ij* source-station couple; and K(f) is a constant depending on the phenomenological coda attenuation. This equation can be linearly inverted for Q_b^{-1}.

2.2 Seismic data

The TOMO-ETNA active experiment generated a large number of seismic signals using air gun shots from aboard the Spanish oceanographic vessel "Sarmiento de Gamboa". The

seismic signals were generated across both the Ionian Sea and the Tyrrhenian Sea and recorded at more than 200 permanent and temporary seismic stations located in Sicily and across the Aeolian volcanic arc (Ibanez et al., 2016a, 2016b). Here, the study area was centered around Mt. Etna; therefore, we only used signals generated in the Ionian Sea and recorded at stations located in the area of interest. In total, we selected 145 seismic stations and 850 seismic sources for use in this study; this allowed us to analyze a total of 1,380,473 seismograms. The selection of seismograms was made according to a series of quality criteria relative to the seismic attributes analyzed (direct wave amplitudes and coda intensity). The coda normalization method requires both a clear, energetic P wave packet and coda amplitudes with a high signal-to-noise ratio. Figure 1 shows a map of the region and an example signal filtered in different frequency bands.

2.2.1 Quality control for seismic signals and data selection

According to Figure 1b and the criteria discussed in the previous section, the proposed method can be applied to signals filtered in several frequency bands. We carried out an extensive analysis of the signal-to-noise ratio to select the optimal frequency band to invert for the P wave attenuation structure of the area. We selected a subset of signals representing all source-station distances and seismic stations. For this subset, the signals were filtered in seven frequency bands (centered at 4, 6, 8, 12, 20, and 24 Hz, with a bandwidth of ± 2 Hz) using a Butterworth band-pass filter with eight poles. According to the dominant source frequency (Coltelli et al., 2016), the spectral content of the seismic signals is very low below 4 Hz. Based on the signal-to-noise ratio, we determined that the best frequency for the analysis was 8 Hz. In the corresponding frequency band, the signal-to-noise ratio is the largest across the whole seismic spectra.

Therefore, we inverted energy ratios from signals filtered between 6 and 10 Hz. After setting this frequency, a systematic study of the signal-to-noise ratio was carried out on the entire dataset, for both the arrivals of the P waves and the coda window. Then, the P/noise, Coda/noise, and P/Coda ratios were calculated. Any signal for which any of these ratios was less than 2 was eliminated.

In summary, the time windows selected for this study included a P wave window with a duration of 1 s from the arrival of the P wave, a coda window beginning 11 s after the arrival of the P wave and with a duration of 2 s, and a window located 5 s before the origin time and with a duration of 5 s, which was used for noise estimation.

As discussed in previous works (e.g., Ibáñez et al., 2020), seismic signals generated with air guns over the sea produce so-called water-waves, whose energy content can alter the seismogram. Since both the propagation speed of this wave packet and the time window of the coda are known, it is possible to theoretically determine which source-station pairs will have the arrival of these waves in the reference coda window. In this way, all data pairs that could have been contaminated by the arrival of the water-wave package in the coda window were eliminated.

After all quality checks, 31,482 traces were retained for the final inversion.

3 P Wave Attenuation Tomography

For the inversion of P-to-coda energy ratios we used the MuRAT1.0 Code (De Siena et al., 2014b). MuRAT is a Matlab©-based tomographic code that measures and inverts the average P and/or S wave quality factors using the method described in the previous section. The most recent release adds tools to invert for the 3D scattering and absorption structure of the area. This

code allows testing of the recovered patterns with checkerboard and synthetic anomaly tests. To obtain our 3D attenuation images, we devised a multi-resolution approach. Tomography was performed on a regional image (lateral extension of 80 x 60 km) with resolution cells of 12 x 12 km, and on a local image centered on the summit zone of Mt. Etna (40 x 40 km with a cell resolution of 6 x 6 km).

3.1 Velocity model and ray tracing

For this inversion, we used a 3D realistic velocity model obtained using joint active-passive seismic tomography by Díaz-Moreno et al. (2018) with spacing of 2 km in both the horizontal and vertical axes. This model takes vertical and lateral heterogeneities into account, giving velocity values for each cell of a defined 3D grid.

The model was used to trace the source-receiver ray-paths obtained using a Thurber-modified ray-bending approach developed by Block (1991). This approach has been applied by De Siena et al. (2010) in Campi Flegrei and Prudencio and Manga (2020) in the Long Valley Caldera, confirming its applicability in volcanic areas despite their high heterogeneity. Figure 2 shows seismic ray density maps in which the number of rays per cell always exceeds five (i.e., the number of rays per cell exceeds the minimum quality standard). In areas of higher density, the number of rays exceeds 1000. For the volcanic area of Mt. Etna, there are between 200 and 300 rays per resolution cell.

3.2 Geometrical spreading

Before solving for the total attenuation variation, it is necessary to set the average geometrical spreading and Q_p^{-1} values. In highly heterogeneous volcanic regions, the geometrical

spreading factor (n) takes a higher value than the theoretical one (2 for 3D media), as shown by Ibáñez et al., (1993) and Akinci et al. (1995a, 1995b). As n and Q_p are coupled, and based on previous studies, the value of geometrical spreading was fixed at n = 2.1.

3.3 Picard condition and l-curve

The MuRAT code from De Siena et al. (2014b) performs a stability test of the Picard condition by comparing singular values with the dot product of the columns of the matrix spanning the data space and the data vector. When the dot products decay to zero more quickly than the singular values, the Picard condition is satisfied. Figure 3a shows the Picard condition for the Mt. Etna data. The dot products (blue line) decay faster than the singular values (red line); therefore, instabilities due to small singular values are unlikely. Figure 3b shows the L-curve used to estimate the damping parameter (α).

3.4 Resolution test

Two types of tests were performed in order to assess (1) the spatial resolution of our data over the entire area (checkerboard test) and (2) to study the capability our data to resolve specific contrasts in attenuation (synthetic anomaly test). For the checkerboard test, we followed a multi-scale procedure developed for a similar active database (Prudencio et al., 2015a). We solved the inversions for regions of different extensions and node spacings, and added Gaussian random noise (10%) to the synthetic energy ratios calculated from a checkerboard synthetic structure. The attenuation contrasts in the synthetic anomaly tests were placed according to the results obtained in the velocity and attenuation tomography studies (Díaz-Moreno et al., 2018 and

Giampiccolo et al., 2020). This allowed us to interpret the details we recovered on these structures.

As indicated above, we divided the study area in two regions—a large region including Mt. Etna and its surroundings (Figure 4) and a smaller area centered on the volcano (Figure 5). For the large region, the data have excellent resolution over an area extending 60 km in an E–W direction and 80 km in a N–S direction; this is consistent with the ray density maps (Figure 2). For the small region, the data have excellent resolution over an area of 40 x 40 km; this coincides with the region of highest ray densities (i.e., > 500 rays per cell; Figure 2).

The resolution tests confirmed that our data for both the larger and smaller regions are very well resolved. Therefore, geological interpretations based on our inversion of the Q_P values can be considered robust.

4 Results and Discussion

4.1 Attenuation model results

The average Qp value of all the energy ratios obtained using a least squares inversion of the coda-normalized energy versus travel time (Figure 6) was 37. This is lower than the values obtained in some other volcanic regions—Prudencio and Manga (2020) obtained a value of 250 for the Long Valley Caldera, and Prudencio et al. (2015b) obtained a value of 125 for the island of Tenerife—but is comparable with those determined by Prudencio et al. (2015a) for Deception Island (29). At Mt. Etna, Martínez-Arévalo et al. (2005) derived a value of 75; the difference between the present study and that of Martínez-Arévalo et al. (2005) reflects the deeper volumes

sampled in the earthquake dataset. Regardless, this value reflects a highly attenuative region, consistent with a heterogeneous area subject to continuous volcanic activity.

Figures 7 and 8 show horizontal projections for the larger and smaller areas of interest, respectively, from 1 km above sea level (a.s.l.; i.e., within the edifice) to 9 km below sea level (b.s.l.). Figures 9 and 10 show two vertical sections (N–S and E–W) passing through the summit zone of Mt. Etna volcano.

In summary, we obtained two 3D models of Mt. Etna. We emphasize that even in the smaller-scale model, we sampled a very large volume compared with previous studies. This was thanks to the high quality of the dataset used, the density of the stations, and the versatility of the method. Even so, the images cannot fully reflect small-scale variation in seismic attenuation; as such, the results are dominated by large structural contrasts. According to the starting Q_P value used for the inversion procedure ($Q_P = 37$) at 8 Hz, we found that the study area is dominated by very high attenuation, as observed in previous studies.

4.2 Large scale attenuation model

In our regional model, there is no clear evidence for *shallow* magma storage beneath Mt. Etna (i.e., there is no apparent contrast with the region surrounding the volcano; Figure 9). However, the model does show regional structural difference, including two zones with opposite attenuation characteristics. To the east of Mt. Etna, in the Ionian Sea, there is a body of low seismic attenuation (high Q_P value) that extends from the surface to at least 7–8 km depth. Although this body reaches the limits of our graphical representation, it is not affected by edge distortion effects and according to the resolution tests it is well resolved. This volume

corresponds to the inferred location of a volcanic shield complex formed before Mt. Etna volcano. This body would be highly consolidated compared with its surroundings, which would explain its low seismic attenuation characteristics. In the same area, Diaz Moreno et al. (2018) highlighted a high-velocity anomaly, located to the south-east of Mt. Etna, compatible with the plumbing system feeding an ancient shield volcano located offshore of the Timpe area (Chiocci et al., 2011; Corsaro et al., 2002). This complex has been hypothesized as the cause of a wide and intense positive magnetic anomaly (> 700 nT) related to deep sources (Cavallaro et al., 2016), as evidenced by a magnetic survey carried out during the TOMO-ETNA experiment; a probable connection between this high-velocity anomaly and the HVB was hypothesized.

A second high Q_P region is located on the north-western edge of study area. Features in this area need to be interpreted with caution owing to partial distortion of the solution. However, previous studies have also shown a high-velocity contrast (Diaz Moreno et al., 2018) area related to different attenuation mechanisms (e.g., low scattering and high intrinsic attenuation; Ibáñez et al., 2020). The strong attenuation contrast (from high-to-low Q_P values), which strikes approximately NE–SW, is consistent with regional tectonic processes acting on the northwestern sector of the volcano. This sector is buttressed against a pre-existing unit, developed in the metamorphic and sedimentary rocks of the Apennine Maghrebian Chain. Therefore, extensive fracturing and seismicity associated with the compressive regime could be responsible for the low-Q_P volume, which correlates well with a low Vp and high Vp/Vs volume observed by Giampiccolo et al. (2020).

4.3 Small scale attenuation model

The most significant result from the second inversion, performed on a smaller volume but with higher resolution, is the presence of a high-attenuation area below the volcano summit. While high attenuation is expected below erupting volcanos, neither a low-velocity nor a high-attenuation volume of this form and dimension have been observed in previous tomographic models of Mt. Etna (e.g., Aloisi et al., 2002; Giampiccolo et al., In Review; Patanè et al., 2006). We believe that this reflects the limitations of regional-scale sampling; even in this study, the larger-scale model failed to identify an anomalous zone below the volcano. To adequately resolve high resolution contrasts, a tomographic inversion must use the most precise starting model available. As shown here, a regional scale active survey provides the necessary attenuation characteristics to highlight fluid- and melt-filled structures.

The morphology of the high-attenuation volume under the volcano is a two-lobed system that moves from E to W when ascending from depth to the surface. The volume develops from ~1 km a.s.l. (i.e., within the edifice) down to ~8 km b.s.l.; the region of maximum attenuation occurs at ~5 km depth. Melts and fluids are associated with abrupt drops in shear wave velocity, and are generally inferred from high Vp/Vs anomalies. However, Giampiccolo et al. (2020) did not observe distinct low VP and high Vp/Vs anomalies in the upper crust beneath the summit craters. Instead, the shallow portion of the volcano is characterized by broad low Vp/Vs anomalies; when associated with low Q anomalies, these can be interpreted as gas-filled volumes (i.e., Giampiccolo et al., 2020).

In addition to this large volume of high attenuation material, we identified three low-attenuation structures, two in the western sector that, as previously discussed, correlate well with high Vp/Vs volumes reported by Giampiccolo et al. (2020), and one south of the summit craters extending from ~6 km b.s.l. to greater depths. The latter may be compatible with the HVB observed in many tomographic models. In our model, this feature does not appear exactly where many other authors represent it, but the location becomes more compatible with depth. Giampiccolo et al. (2020) found that the upper part of the HVB has persistent low Vp/Vs anomalies which, together with high the V_p and low Q_P, suggest the presence of broad gas-dominated volumes within the upper portion of the body.

Finally, we identified small volumes with high Q_P values in the western sector of the volcano; these were also observed in the regional model, albeit less intense (Figure 7, Figure 9). In this sector of the volcano, volumes with high Q-coda values have been observed in other studies (Giampiccolo et al., In Review) and were associated with seismically active fault structures. However, comparing our results with those of previous studies (Díaz-Moreno et al., 2018; Giampiccolo et al., 2020 and references therein; Ibáñez et al., 2020), this area contains different volumes with low and high anomalies in terms of both velocity and attenuation. Since each previous model analyses a different type of wave and/or propagation processes, the directions of the anomalies also differ. However, the widespread consensus that different seismic and volcanic processes are occurring in this area is consistent with our observations. In particular, one of the most accepted explanations is the presence of over-pressurized regions resulting from aquifers embedded in the system and affected by volcanic heat flow (i.e., Giampiccolo et al., 2020). This could explain observations of multiple volumes with low seismic

velocities (Aloisi et al., 2002; Díaz-Moreno et al., 2018; Giampiccolo et al., 2020), high scattering attenuation (Ibáñez et al., 2020), but low attenuation of P waves.

Figure 11 shows a 3D representation of the shallowest of these attenuation bodies. The position and shape are compatible with the presence of molten or partially molten material (magma) that feeds the eruptive processes observed at Mt. Etna volcano.

4.4 Joint interpretation

Figure 12 shows the joint interpretation of four different tomographic models of the Mt. Etna area, including two velocity tomography models (Díaz-Moreno et al., 2018; Giampiccolo et al., 2020) and two attenuation models, one using coda waves (Giampiccolo et al., In Review) and one presented in this study. Our joint interpretation takes into account the Vp of the two different 3D models, the Vp/Vs from the tomography results, and two attenuation values Qc, Qp derived from the present study.

Eight main structures are depicted in Figure 12.

1. Highly consolidated structure. This region (marked in dark blue) is characterized by high Vp, high Vp/Vs ratios, high Qc values, and an average Q_P value. This feature is consistent with the consolidated crystalline basement. In addition, a small highly consolidated volume is evident in the shallow crust beneath the volcano; it is consistent with the well-known HVB.

2. Consolidated structure. A consolidated structure (depicted in light blue) has similar characteristics to the highly consolidated structure, but both the Qc and Qp are of average values. It is possible that these structures have similar geological interpretations, but that the resolutions of the attenuation studies allowed for their differentiation.

3. Transition zone. A transition zone (depicted in deep purple) was assigned as such because it is located in an intermediate region between the highly consolidated area and a region containing molten material. This volume has high seismic attenuation (low Q); however, the velocity propagation values are still compatible with a consolidated body. This feature may represent a high temperature rock, adjacent to the magma storage region, with altered physical properties.

4. High pressure fluids. We identified three volumes (depicted in pink) with low Vp, high Vp/Vs (and therefore very low Vs), and average low Q values. Some of these areas can be considered as potential reservoirs of over-pressurized fluids, as described by Giampiccolo et al. (2020).

5. Melt. This structure (depicted in red) is consistent with the presence of fluids; given the nature of this volcanic environment, we interpret this to be a region of magma storage in the shallower crust below Mt. Etna. The structure has a large volume (at least 450 km^3), revealing a large eruptive potential. At the time of writing (March 2021), Mt. Etna volcano is undergoing a new and very energetic eruptive process.

6. Volcanoclastic materials. We identified two very shallow areas (depicted in orange and dark orange) that are consistent with volcanoclastic materials (e.g., lava flows and ash deposits). The two bodies show slight differences in their physical properties, although this may reflect the resolution limits of the analysis methods.

7. Sediments. We interpreted an third area (depicted in yellow), with physical properties similar to those of the volcaniclastic materials, to be sediments, based on evidence from local geological studies (Giampiccolo et al., 2020).

8. Unknown. We identified one structural element (depicted in turquoise) for which we have no interpretation. This structure has high Vp values but low Vp/Vs and average to low Q values. In general, this area is consistent with a consolidate material with plastic properties.

Our results confirm the remarkable complexity of the geological structure beneath Mt. Etna. It is likely that this complexity is common to other stratovolcanoes too; however, without the abundance of data from multiple studies that contribute to Mt. Etna as a laboratory volcano, such observations and interpretations would not be possible. Further insight in this high structural complexity will require new advances in data and methods, which in turn will improve our understanding of volcano structures and help us to better constrain their behavior.

5 Conclusions

Volcanoes are highly heterogeneous structures; at present, tomographic images based on velocity and attenuation are some of the most powerful tools available for investigating their complex structures and behaviors. Several techniques can be used to obtain these images, with each revealing different physical properties of the medium and each having different resolution limits. Although these models aim to associate physical properties with geological structures, in most cases individual images can only partially reveal the sub-surface volcanic system. This limits interpretations and introduces uncertainties.

Here, we have presented a new attenuation-based tomographic model derived using P waves from an active seismic experiment; this method has not previously been applied at Mt. Etna. We used a sufficiently large data volume to cover the Mt. Etna region to a depth of 8 km. These new images reveal a large volume of molten material in the very shallow crust beneath Mt. Etna. During the investigated period, Mt. Etna was characterized by several episodes of Strombolian activity and lava emissions from the main upper craters (i.e., Viccaro et al. 2016 and references therein). Our results provide a visualization of the magmatic source feeding these eruptive episodes. Integrated analysis of geodetic, seismic, and petrological data suggests that magma stored at ~4 km b.s.l. drove the eruptive activity of July–August 2014; this body of melt was fed by a batch of magma that starting ascending from > 8 km depth in late 2013 (Viccaro et al., 2016). This magmatic reservoir is considered as the region of neutral buoyancy at Mt. Etna (Corsaro & Pompilio, 2004).

To better constrain the main geological framework of this volcano, we performed a joint interpretation of recent velocity and attenuation tomographies performed by our research team. The results confirm the presence of several different geological bodies, and provide a new and more complete picture of the inner structure of Mt. Etna volcano. In particular, we identified a large shallow region below the summit area that is consistent with the presence of fluids. We interpret this to represent a large area of shallow magma storage. This finding confirms the significant eruptive potential of Mt. Etna volcano. Our results provide new insights into the volcanic system at Mt. Etna, and have the potential to inform on present and future eruptive behavior. Moreover, we have confirmed that the joint interpretation of different models provides a useful tool for the study of volcanic systems.

Acknowledgments

This study was partially supported by the Spanish FEMALE project (PID2019-106260GB-I00). We would like to thank Dr. Luca de Siena for assistance using the Murat software and for providing a review of the present manuscript. English gramma and review have been performed by the Tornillo Scientific (UK) company.

Data

Seismic data used in the present work are available in the following data repositoty:

https://geofon.gfz-potsdam.de/doi/network/1T/2014

This data base must be cited as: Ibanez, Jesus M.; Lühr, Birger ; Dahm, Torsten (2014): TOMO-ETNA. GFZ Data Services. Other/Seismic Network. doi:10.14470/6G7569676919.

References

Aki, K. (1980). Scattering and attenuation of shear waves in the lithosphere. Journal of Geophysical Research: Solid Earth, 85(B11), 6496-6504.

Akinci, A., Ibanez, J. M., Del Pezzo, E., & Morales, J. (1995a), Geometrical spreading and attenuation of Lg waves: a comparison between western Anatolia (Turkey) and southern Spain. *Tectonophysics*, *250*(1–3), 47–60.

Akinci, A., Del Pezzo, E., & Ibanez, J. M. (1995b), Separation of scattering and intrinsic attenuation in southern Spain and western Anatolia (Turkey). *Geophysical Journal International, 121*(2), 337–353.

Aloisi, M., Bonaccorso, A., Cannavò, F., Currenti, G., & Gambino, S. (2020), The 24 December 2018 eruptive intrusion at Etna volcano as revealed by multidisciplinary continuous deformation networks (CGPS, Borehole Strainmeters and Tiltmeters). *Journal of Geophysical Research: Solid Earth, 125*(8), e2019JB019117.

Aloisi, M., Cocina, O., Neri, G., Orecchio, B., & Privitera, E. (2002), Seismic tomography of the crust underneath the Etna volcano, Sicily. *Physics of the Earth and Planetary Interiors, 134*(3–4), 139–155.

Alparone, S., Maiolino, V., Mostaccio, A., Scaltrito, A., Ursino, A., Barberi, G., et al. (2015), Instrumental seismic catalogue of Mt. Etna earthquakes (Sicily, Italy): ten years (2000–2010) of instrumental recordings. *Annals of Geophysics, 58*(4), 0435.

Azzaro, R., Branca, S., Gwinner, K., & Coltelli, M. (2012). The volcano-tectonic map of Etna volcano, 1: 100.000 scale: an integrated approach based on a morphotectonic analysis from high-resolution DEM constrained by geologic, active faulting and seismotectonic data. *Italian Journal of Geosciences, 131*(1), 153–170.

Barberi, G., Giampiccolo, E., Musumeci, C., Scarfì, L., Bruno, V., Cocina, O., et al. (2016), Seismic and volcanic activity during 2014 in the region involved by TOMO-ETNA seismic active experiment. *Annals of Geophysics. 59*. https://doi.org/10.4401/ag-7082.

Barreca, G., Branca, S., Corsaro, R. A., Scarfì, L., Cannavò, F., Aloisi, M., et al. (2020), Slab detachment, mantle flow, and crustal collision in eastern Sicily (southern Italy): Implications on Mount Etna volcanism. *Tectonics, 39*(9), e2020TC006188.

Barreca, G., Branca, S., & Monaco, C. (2018). Three−Dimensional Modeling of Mount Etna Volcano: Volume Assessment, Trend of Eruption Rates, and Geodynamic Significance. *Tectonics, 37*(3), 842–857.

Basant, R. A., Ryan, G. A., Peacock, J. R., Camacho, A. G., Blake, O. O., Hautmann, S., & Lynne, B. Y. (2021), Multi-geophysical parameter classification of the Montserrat geothermal system. *Geothermics, 90*, 102006.

Ben-Zvi, T., Wilcock, W. S., Barclay, A. H., Zandomeneghi, D., Ibáñez, J. M., & Almendros, J. (2009), The P-wave velocity structure of Deception Island, Antarctica, from two-dimensional seismic tomography. *Journal of Volcanology and Geothermal Research, 180*(1), 67–80.

Block, L. V. (1991), *Joint hypocenter−velocity inversion of local earthquakes arrival time data in two geothermal regions*, (Doctoral thesis). Cambridge: Massachusetts Institute of Technology.

Bonforte, A., Bonaccorso, A., Guglielmino, F., Palano, M., & Puglisi, G. (2008). Feeding system and magma storage beneath Mt. Etna as revealed by recent inflation/deflation cycles. Journal of Geophysical Research: Solid Earth, 113(B5).

Branca, S., & Ferrara, V. (2013), The morphostructural setting of Mount Etna sedimentary basement (Italy): Implications for the geometry and volume of the volcano and its flank instability. *Tectonophysics, 586*, 46–64.

Cavallaro, D., Cocchi, L., Coltelli, M., Muccini, F., Carmisciano, C., Firetto Carlino, M., et al. (2016), Acquisition procedures, processing methodologies and preliminary results of magnetic and ROV data collected during the TOMO-ETNA experiment. *Annals of Geophysics, 59*(4).

Chiarabba, C., De Gori, P., & Patanè, D. (2004), The Mt. Etna plumbing system: the contribution of seismic tomography. In A. Bonaccorso, S. Calvari, M. Coltelli, C. DelNegro, S. Falsaperla (Eds.), *Etna volcano laboratory*, *Geophysical Monograph Series* (pp. 191–204). Washington, DC: American Geophysical Union

Chiocci, F. L., Coltelli, M., Bosman, A., & Cavallaro, D. (2011), Continental margin large-scale instability controlling the flank sliding of Etna volcano. *Earth and Planetary Science Letters, 305*(1–2), 57–64.

Coltelli, M., Cavallaro, D., Firetto Carlino, M., Cocchi, L., Muccini, F., D'Aessandro, A., et al. (2016), The marine activities performed within the TOMO-ETNA experiment. *Annals of Geophysics, 59*(4).

Cordell, D., Unsworth, M. J., Lee, B., Díaz, D., Bennington, N. L., & Thurber, C. H. (2020), Integrating magnetotelluric and seismic images of silicic magma systems: A case study from the Laguna del Maule Volcanic Field, central Chile. *Journal of Geophysical Research: Solid Earth, 125*(11), e2020JB020459.

Corsaro, R. A., & Pompilio, M. (2004). Buoyancy‐controlled eruption of magmas at Mt Etna. Terra Nova, 16(1), 16-22.

Corsaro, R. A., Neri, M., & Pompilio, M. (2002), Paleo-environmental and volcano-tectonic evolution of the southeastern flank of Mt. Etna during the last 225 ka inferred from the volcanic

succession of the 'Timpe', Acireale, Sicily. *Journal of Volcanology and Geothermal Research, 113*(1–2), 289–306.

De Gori, P., Chiarabba, C., Giampiccolo, E., Martinez–Arèvalo, C., & Patanè, D. (2011), Body wave attenuation heralds incoming eruptions at Mount Etna. *Geology, 39*(5), 503–506.

De Guidi, G., Barberi, G., Barreca, G., Bruno, V., Cultrera, F., Grassi, S., et al. (2015), Geological, seismological and geodetic evidence of active thrusting and folding south of Mt. Etna (eastern Sicily): Revaluation of "seismic efficiency" of the Sicilian Basal Thrust. *Journal of geodynamics, 90*, 32–41.

Del Pezzo, E., Bianco, F., De Siena, L., & Zollo, A. (2006), Small scale shallow attenuation structure at Mt. Vesuvius, Italy. *Physics of the Earth and Planetary Interiors, 157*(3–4), 257–268.

De Siena, L., Amoruso, A., Pezzo, E. D., Wakeford, Z., Castellano, M., & Crescentini, L. (2017), Space−weighted seismic attenuation mapping of the aseismic source of Campi Flegrei 1983–1984 unrest. *Geophysical Research Letters, 44*(4), 1740–1748.

De Siena, L., Del Pezzo, E., & Bianco, F. (2010), Seismic attenuation imaging of Campi Flegrei: Evidence of gas reservoirs, hydrothermal basins, and feeding systems. *Journal of Geophysical Research: Solid Earth, 115*(B9).

De Siena, L., Thomas, C., & Aster, R. (2014b), Multi-scale reasonable attenuation tomography analysis (MuRAT): An imaging algorithm designed for volcanic regions. *Journal of Volcanology and Geothermal Research, 277*, 22–35.

De Siena, L., Thomas, C., Waite, G. P., Moran, S. C., & Klemme, S. (2014a), Attenuation and scattering tomography of the deep plumbing system of Mount St. Helens. *Journal of Geophysical Research: Solid Earth, 119*(11), 8223–8238.

Díaz-Moreno, A., Barberi, G., Cocina, O., Koulakov, I., Scarfì, L., Zuccarello, L., et al. (2018), New insights on Mt. Etna's crust and relationship with the regional tectonic framework from joint active and passive P-wave seismic tomography. *Surveys in Geophysics, 39*(1), 57–97.

Díaz-Moreno, A., Koulakov, I., García-Yeguas, A., Jakovlev, A., Barberi, G., Cocina, O., et al. (2016), PARTOS-Passive and Active Ray TOmography Software: description and preliminary analysis using TOMO-ETNA experiment's dataset. *Annals of Geophysics, 59*(4).

García, L., Álvarez, I., Benítez, C., Titos, M., Bueno, Á., Mota, S., et al. (2016), Advances on the automatic estimation of the P-wave onset time. *Annals of Geophysics, 59*(4), 0434.

García−Yeguas, A., Koulakov, I., Ibáñez, J. M., & Rietbrock, A. (2012). High resolution 3D P wave velocity structure beneath Tenerife Island (Canary Islands, Spain) based on tomographic inversion of active−source data. *Journal of Geophysical Research: Solid Earth, 117*(B9).

García-Yeguas, A., Ledo, J., Piña-Varas, P., Prudencio, J., Queralt, P., Marcuello, A., et al. (2017), A 3D joint interpretation of magnetotelluric and seismic tomographic models: The case of the volcanic island of Tenerife. *Computers & Geosciences, 109*, 95–105.

Giampiccolo, E., Cocina, O., De Gori, P., & Chiarabba, C. (2020), Dyke intrusion and stress-induced collapse of volcano flanks: The example of the 2018 event at Mt. Etna (Sicily, Italy). *Scientific Reports, 10*(1), 1–8.

Giampiccolo, E. Del Pezzo, E., Tuvé, T., Di Grazia, S., & Ibáñez, J.M. (2021), Kernel-based 3-D Q-coda attenuation structure at Mt. Etna. Acepted to be published *Geophysical Journal International*.

Guardo, R., & De Siena, L. (2017), Integrating ambient noise with GIS for a new perspective on volcano imaging and monitoring: The case study of Mt. Etna. *Journal of Volcanology and Geothermal Research, 347*, 397–407.

Guardo, R., De Siena, L., & Dreidemie, C. (2020), Mt. Etna Feeding System and Sliding Flank: A New 3D Image From Earthquakes Distribution in a Customisable GIS. *Frontiers in Earth Sciences, 8*, 1–12

Ibáñez, J. M., Castro-Melgar, I., Cocina, O., Zuccarello, L., Branca, S., Del Pezzo, E., & Prudencio, J. (2020), First 2-D intrinsic and scattering attenuation images of Mt Etna volcano and surrounding region from active seismic data. *Geophysical Journal International, 220*(1), 267–277.

Ibáñez, J. M., Del Pezzo, E., Alguacil, G., De Miguel, F., Morales, J., De Martino, S., et al. (1993), Geometrical spreading function for short-period S and coda waves recorded in southern Spain. *Physics of the Earth and Planetary Interiors, 80*(1–2), 25–36.

Ibáñez, J. M., Prudencio, J., Díaz-Moreno, A., Patanè, D., Puglisi, G., Lühr, B. G., et al. (2016a), The TOMO-ETNA experiment: an imaging active campaign at Mt. Etna volcano. Context, main objectives, working-plans and involved research projects. *Annals of Geophysics, 59*(4), 0426.

Ibáñez, J. M., Díaz-Moreno, A., Prudencio, J., Patené, D., Zuccarello, L., Cocina, O., et al. (2016b). TOMO-ETNA experiment at Etna volcano: activities on land. Annals of Geophysics, 59(4).

Ibáñez, J. M., Rietbock, A., & García−Yeguas, A. (2008), Imaging an active volcano edifice at Tenerife Island, Spain. *Eos Transactions, 89*(32), 289–290.

Koulakov, I., Smirnov, S. Z., Gladkov, V., Kasatkina, E., West, M., El Khrepy, S., & Al-Arifi, N. (2018), Causes of volcanic unrest at Mt. Spurr in 2004–2005 inferred from repeated tomography. *Scientific Reports, 8*(1), 1–7.

Koulakov, I., & Vargas, C. A. (2018), Evolution of the magma conduit beneath the Galeras volcano inferred from repeated seismic tomography. *Geophysical Research Letters, 45*(15), 7514–7522.

Laiolo, M., Ripepe, M., Cigolini, C., Coppola, D., Della Schiava, M., Genco, R., et al. (2019), Space-and ground-based geophysical data tracking of magma migration in shallow feeding system of mount Etna volcano. *Remote Sensing, 11*(10), 1182.

Martinez-Arevalo, C., Patanè, D., Rietbrock, A. & Ibáñez, J. (2005), The intrusive process leading to the Mt. Etna 2001 flank eruption: Constraints from 3D attenuation tomography. *Geophysical Research Letters, 32*, https://doi.org/10.1029/2005GL023736

Neri, M., Casu, F., Acocella, V., Solaro, G., Pepe, S., Berardino, P., et al. (2009), Deformation and eruptions at Mt. Etna (Italy): A lesson from 15 years of observations. *Geophysical Research Letters, 36*(2).

Patanè, D., Barberi, G., Cocina, O., De Gori, P., & Chiarabba, C. (2006), Time-resolved seismic tomography detects magma intrusions at Mount Etna. *Science, 313*(5788), 821–823.

Patanè, D., Chiarabba, C., Cocina, O., De Gori, P., Moretti, M., & Boschi, E. (2002), Tomographic images and 3D earthquake locations of the seismic swarm preceding the 2001 Mt. Etna eruption: evidence for a dyke intrusion. *Geophysical Research Letters, 29*, 10. https://doi.org/10.1029/2001GL014391.

Presti, D. L., Riggi, F., Ferlito, C., Bonanno, D. L., Bonanno, G., Gallo, G., et al. (2020), Muographic monitoring of the volcano-tectonic evolution of Mount Etna. *Scientific Reports, 10*(1), 1–11.

Prudencio, J., Del Pezzo, E., García-Yeguas, A., & Ibáñez, J. M. (2013a). Spatial distribution of intrinsic and scattering seismic attenuation in active volcanic islands–I: model and the case of Tenerife Island. Geophysical Journal International, 195(3), 1942-1956.

Prudencio, J., Ibánez, J. M., García-Yeguas, A., Del Pezzo, E., & Posadas, A. M. (2013b). Spatial distribution of intrinsic and scattering seismic attenuation in active volcanic islands–II: Deception Island images. Geophysical Journal International, 195(3), 1957-1969.

Prudencio, J., De Siena, L., Ibáñez, J. M., Del Pezzo, E., Garcia-Yeguas, A., & Diaz-Moreno, A. (2015a), The 3D attenuation structure of Deception Island (Antarctica). *Surveys in Geophysics, 36*(3), 371–390.

Prudencio, J., Ibáñez, J. M., Del Pezzo, E., Martí, J., García-Yeguas, A., & De Siena, L. (2015b), 3D attenuation tomography of the volcanic island of Tenerife (Canary Islands). *Surveys in Geophysics, 36*(5), 693–716.

Prudencio, J., & Manga, M. (2020), 3-D seismic attenuation structure of Long Valley caldera: looking for melt bodies in the shallow crust. *Geophysical Journal International, 220*(3), 1677–1686.

Shalev, E., Kenedi, C. L., Malin, P., Voight, V., Miller, V., Hidayat, D., et al. (2010), Three‐dimensional seismic velocity tomography of Montserrat from the SEA‐CALIPSO offshore/onshore experiment. *Geophysical Research Letters, 37*(19).

Viccaro, M., Barca, D., Bohrson, W. A., D'Oriano, C., Giuffrida, M., Nicotra, E., & Pitcher, B. W. (2016). Crystal residence times from trace element zoning in plagioclase reveal changes in magma transfer dynamics at Mt. Etna during the last 400 years. Lithos, 248, 309-323.

Voight, B., Sparks, R. S. J., Shalev, E., Minshull, T., Paulatto, M., Annen, C., et al. (2014), The SEA-CALIPSO volcano imaging experiment at Montserrat: plans, campaigns at sea and on land, scientific results, and lessons learned. *Geological Society, London, Memoirs, 39*(1), 253–289.

Yoshimoto, K., Sato, H., & Ohtake, M. (1993), Frequency‐dependent attenuation of P and S waves in the Kanto area, Japan, based on the coda‐normalization method, *Geophysics Journal International, 114*, 165–174.

Zandomeneghi, D., Barclay, A., Almendros, J., Ibáñez, J. M., Wilcock, W. S., & Ben‐Zvi, T. (2009), Crustal structure of Deception Island volcano from P wave seismic tomography: Tectonic and volcanic implications. *Journal of Geophysical Research: Solid Earth, 114*(B6).

FIGURE CAPTION

Figure 1. Study region location and an example signal filtered at multiple frequencies. (**a**) Map of the study region, with seismic stations represented by red triangles and explosions or air gun shots represented by blue pluses; inset maps show the regional location of Mt. Etna (upper left-hand side) and the active craters of Mt. Etna (lower left-hand side; BN, Bocca Nuova; VOR, Voragine; NEC, North East crater; SEC, South East crater; NSEC, New South East Crater). (**b**) Example signal filtered at multiple frequencies; this signal was generated by an explosion (light blue dot in part 'a') and recorded at a station near Mt. Etna (yellow triangle in part 'a'). The seismic signal is filtered every 4 Hz, from 4 to 24 Hz. The lower plot compares the spectrum of the signal with that of the pre-event noise. The 8 Hz frequency band (shown in light blue) was selected for this study because it presents the best signal-to-noise ratio.

Figure 2. Seismic ray density maps of Mt. Etna at different depths. Densities are represented as a function of the sampled depth, and the number of rays per cell always exceeds five.

Figure 3. Picard condition and L-curve of the Mt. Etna data. (**a**) Picard condition plot, in which dot products (blue curve) decay to zero more quickly than the singular values (red curve) and the Picard condition is satisfied. (**b**) L-curve used to estimate the damping parameter (α) for the inversion.

Figure 4. Results of checkerboard and localized synthetic anomaly resolution tests carried out to determine the resolution and sensitivity of our tomographic study. Checkerboard and localized synthetic anomaly resolution test results for a large region that comprises Mt. Etna and the surrounding area using cells of 12 x 12 km. In the central column we present the input model for the localized synthetic anomaly resolution test.

Figure 5. Results of checkerboard and localized synthetic anomaly resolution tests carried out to determine the resolution and sensitivity of our tomographic study. Checkerboard and localized synthetic anomaly resolution test results for a small region centered over Mt. Etna (cells of 6 x 6 km). In the central column we present the input model for the localized synthetic anomaly resolution test.

Figure 6. Fit of coda-normalized energy ratios versus travel time. The red line is the best mean square fit, from which we obtained the average Q-value for the Mt. Etna region.

Figure 7. Tomographic images of the region around Mt. Etna volcano in different horizontal layers, from 1 km above sea level (i.e., within the edifice) to 9 km below sea level (the resolution limit).

Figure 8. Tomographic images of Mt. Etna volcano in different horizontal layers, from 1 km above sea level (i.e., within the edifice) to 9 km below sea level (the resolution limit).

Figure 9. North–south (A–A') and east–west (B–B') vertical sections across the Mt. Etna region. The locations of A–A' and B–B' are shown in Figure 7.

Figure 10. North–south (C–C') and east–west (D–D') vertical sections across Mt. Etna volcano. The locations of C–C 'and D–D' are shown in Figure 8.

Figure 11. Three-dimensional (3D) attenuation model of the shallowest attenuation body identified beneath Mt. Etna volcano.

Figure 12. Schematic view of the structure beneath Mt. Etna volcano based on the joint interpretation of four different tomographic models of attenuation and velocity. HVB, High Velocity Body.

FIGURES

Figure 1

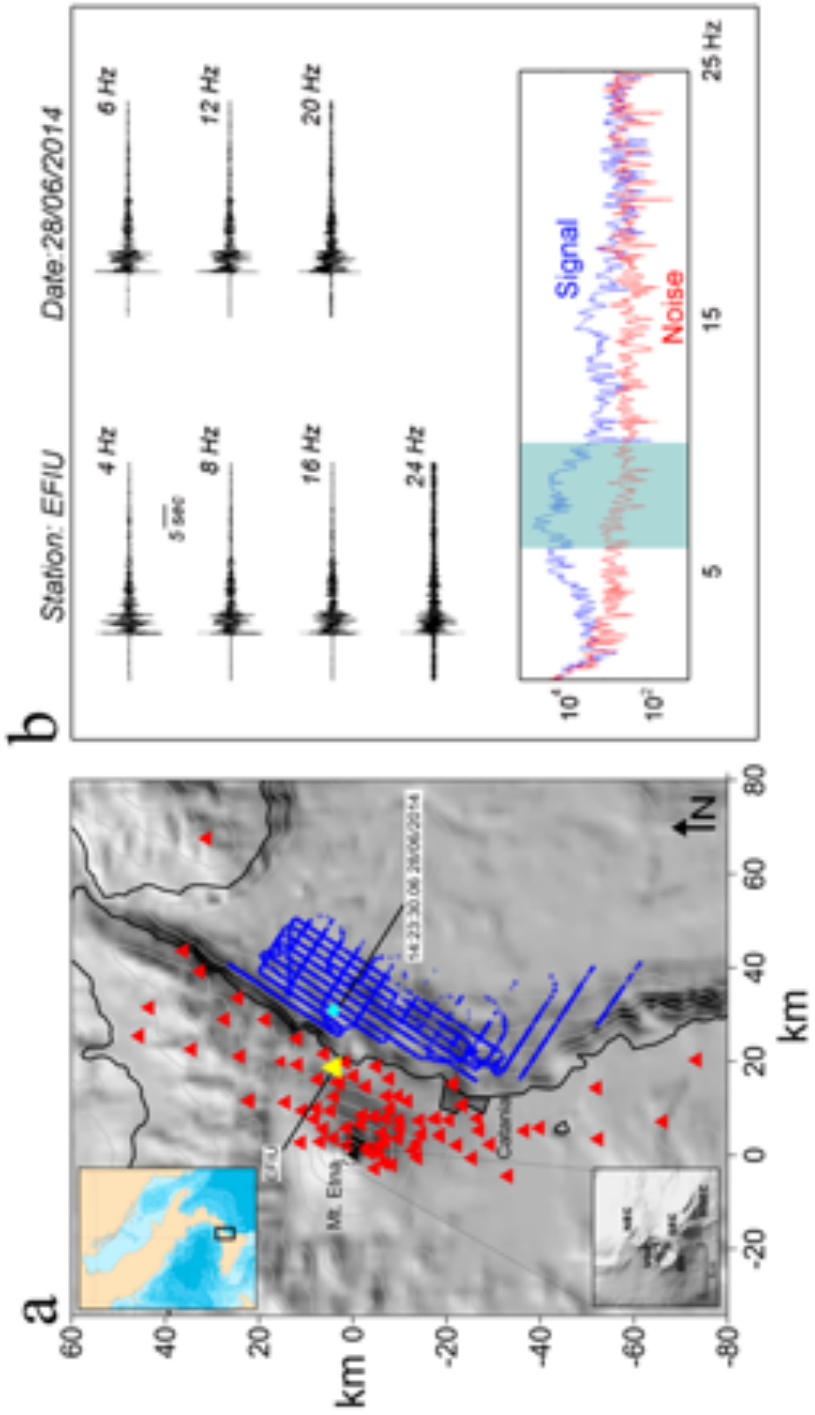
b
Station: EFIU
Date:28/06/2014
4 Hz
8 Hz
16 Hz
24 Hz
6 Hz
12 Hz
20 Hz
5 sec
Signal
Noise
10^-1
10^-2
5
15
25 Hz
a
km
60
40
20
0
-20
-40
-60
-80
N
Mt. Etna
Catania
EFIU
14:23:30.06 28/06/2014

Figure 2

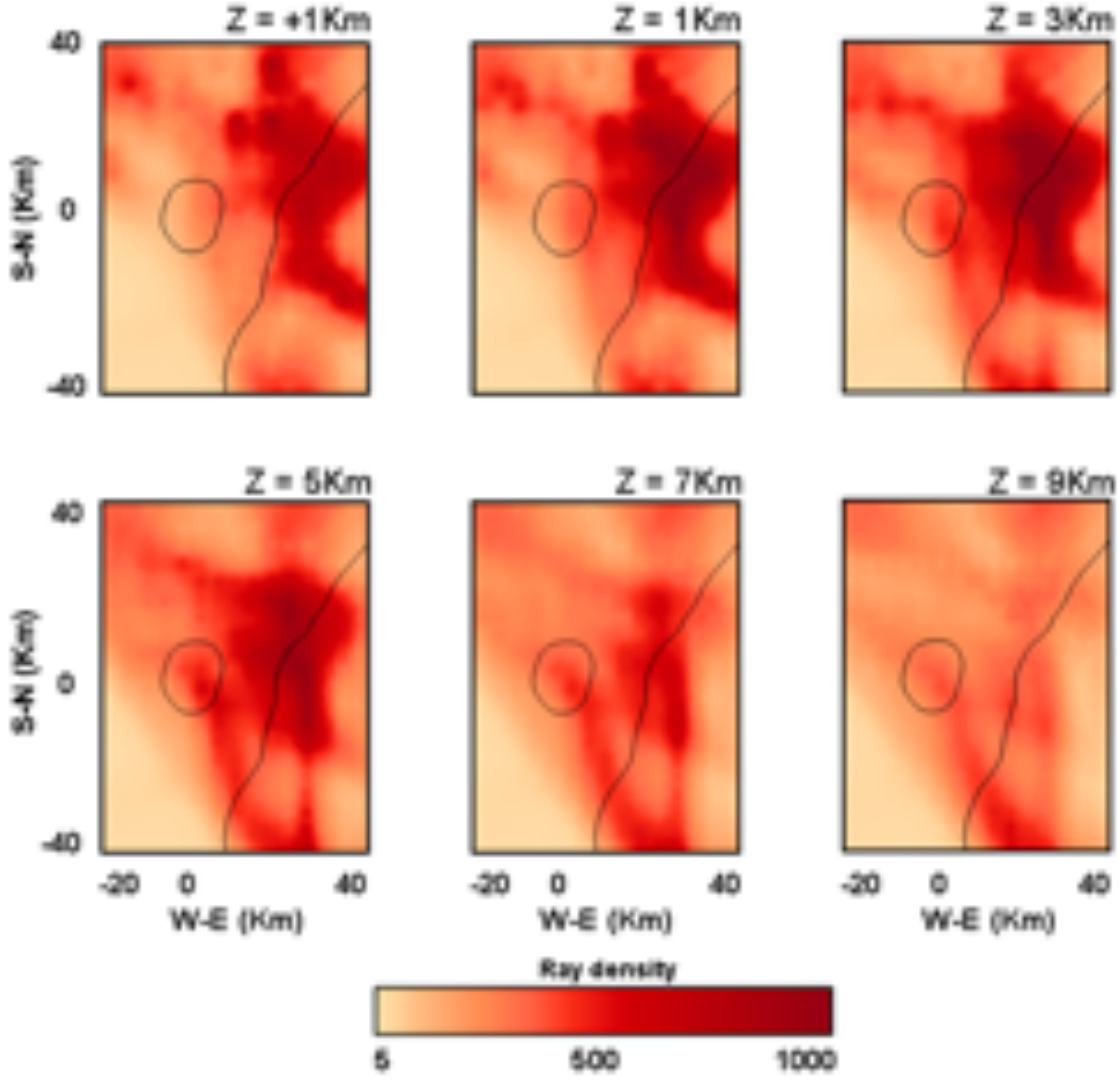
Z = +1Km
Z = 1Km
Z = 3Km
Z = 5Km
Z = 7Km
Z = 9Km
S-N (Km)
40
0
-40
-20
0
40
W-E (Km)
Ray density
5
500
1000

Figure 3

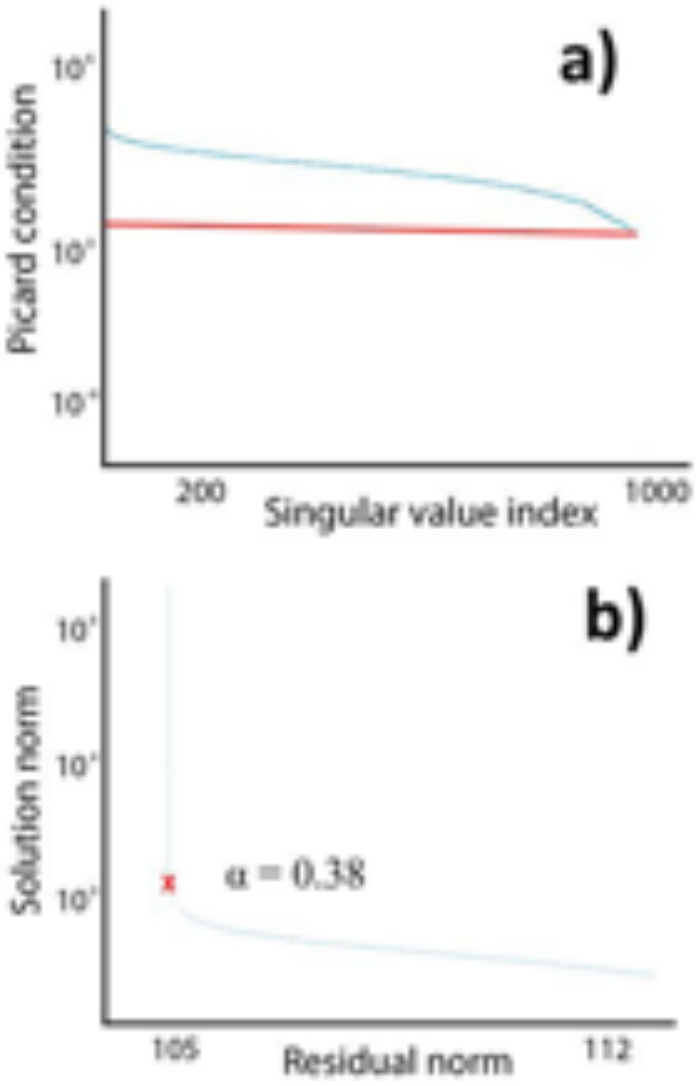
a)
Picard condition
200
Singular value index
1000
b)
Solution norm
α = 0.38
105
Residual norm
112

Figure 4

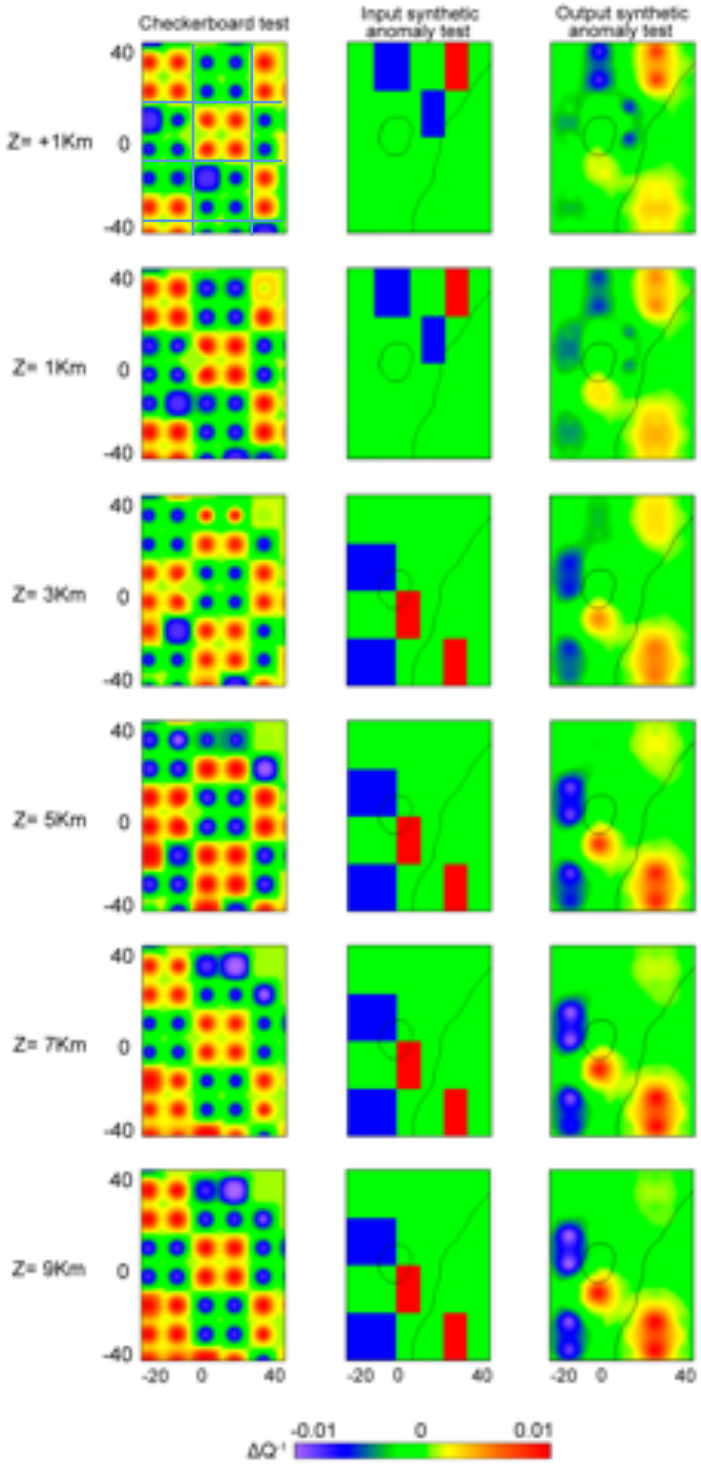
Checkerboard test
Input synthetic anomaly test
Output synthetic anomaly test
Z= +1Km
Z= 1Km
Z= 3Km
Z= 5Km
Z= 7Km
Z= 9Km
40
0
-40
-20
0
40
-0.01
0
0.01
ΔQ⁻¹

Figure 5

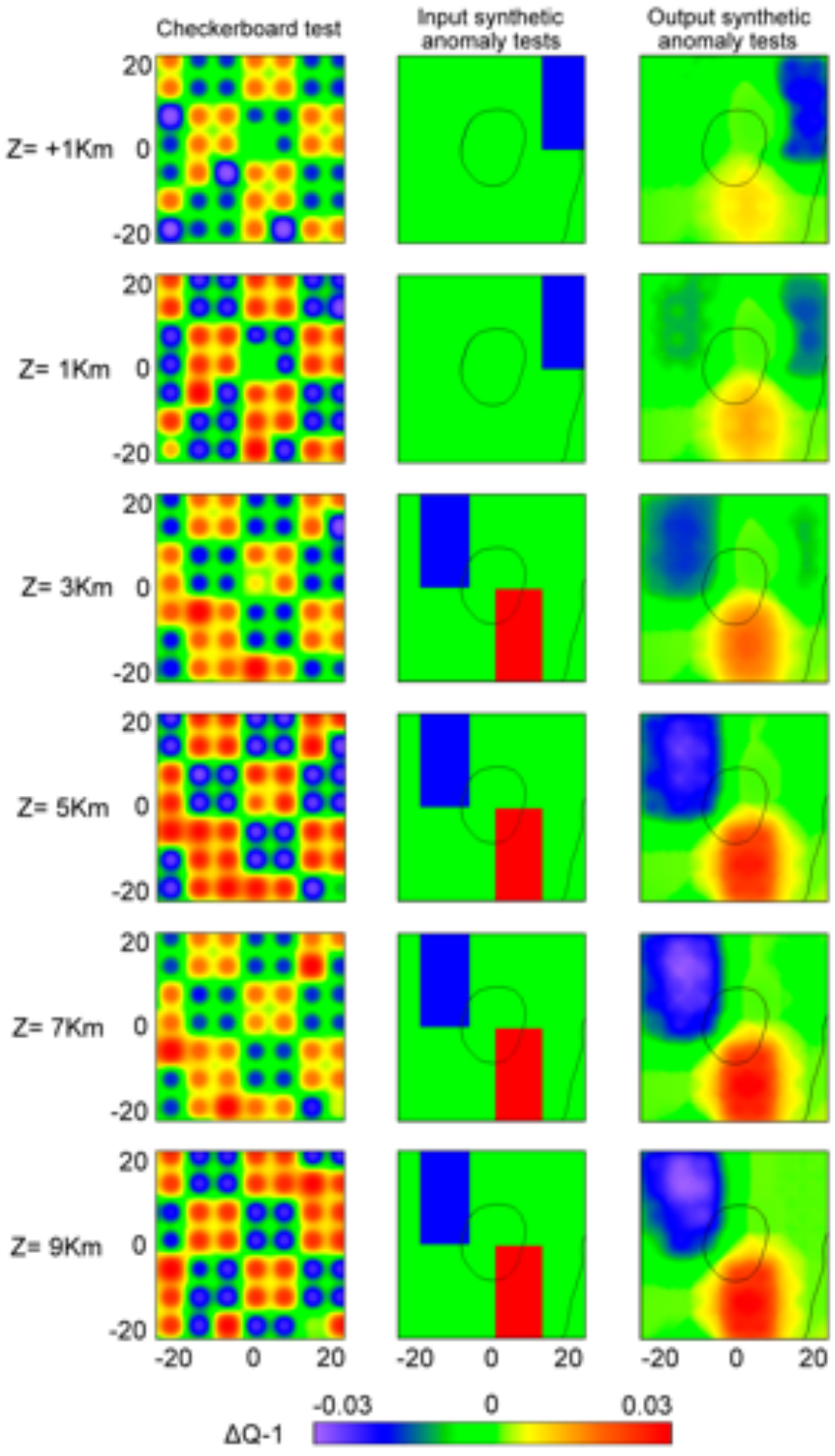
Checkerboard test
Input synthetic anomaly tests
Output synthetic anomaly tests
Z= +1Km
Z= 1Km
Z= 3Km
Z= 5Km
Z= 7Km
Z= 9Km
20
0
-20
-0.03
0
0.03
ΔQ-1

Figure 6

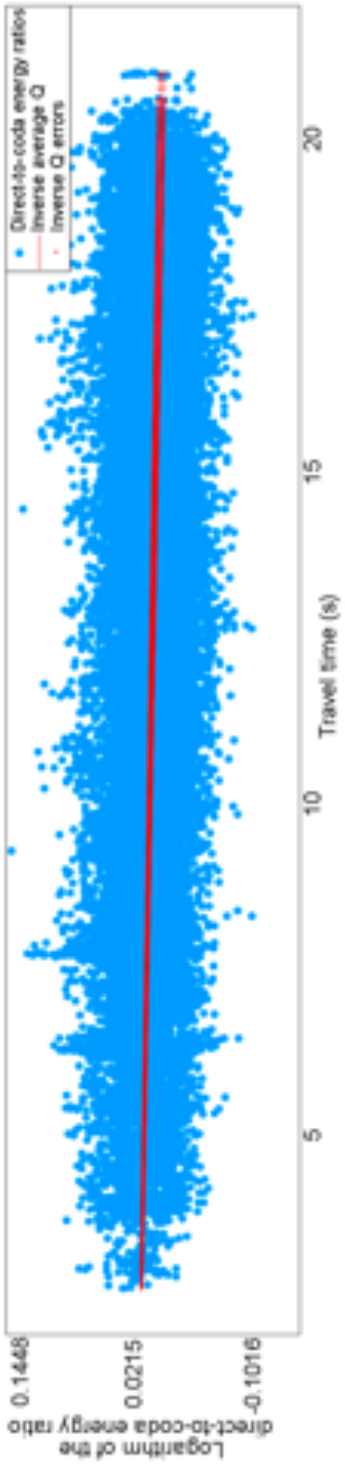
Direct-to-coda energy ratio
Inverse average Q
Inverse Q errors
0.1448
0.0215
-0.1016
Logarithm of the direct-to-coda energy ratio
5
10
15
20
Travel time (s)

Figure 7

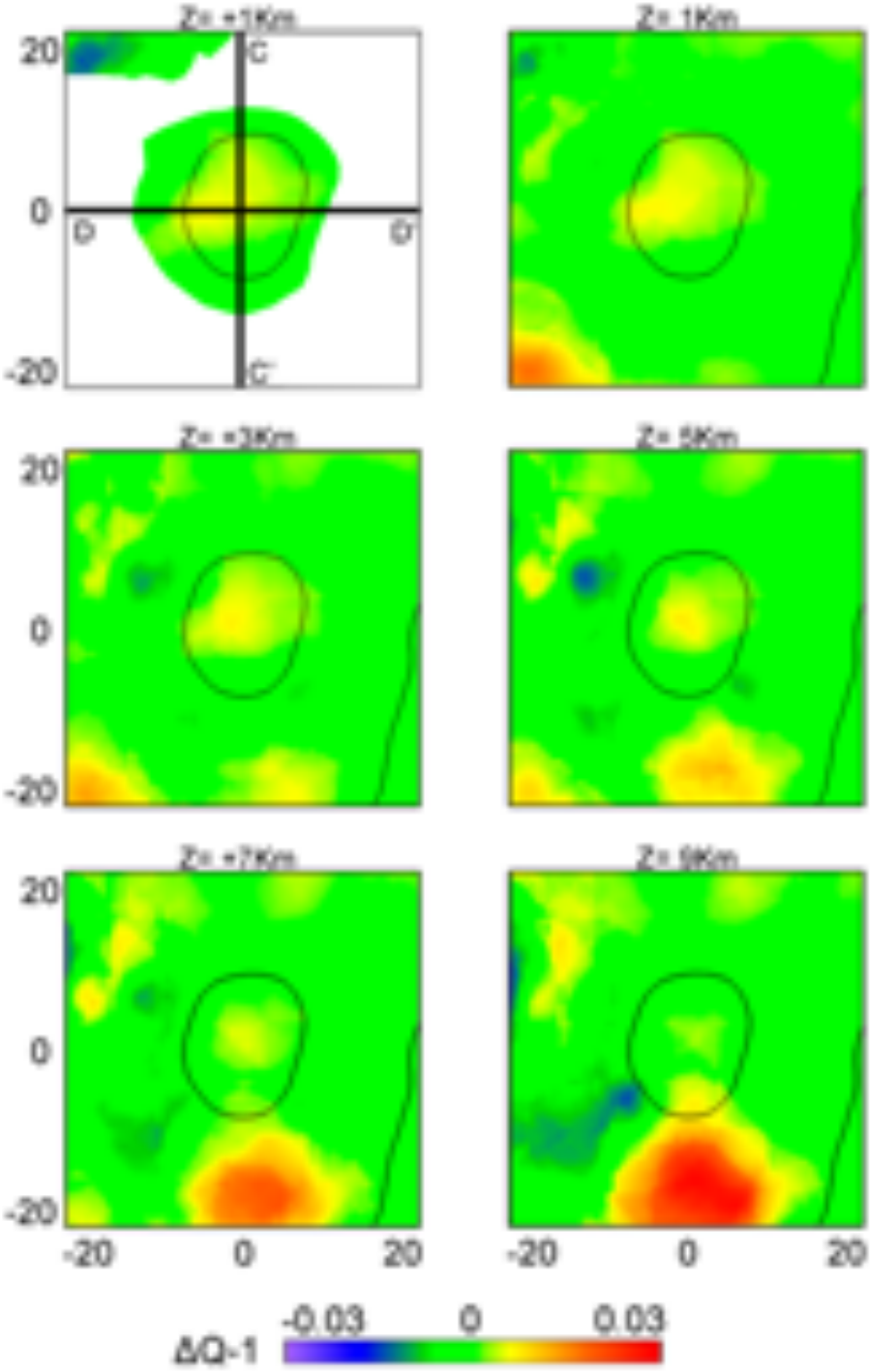

Figure 8

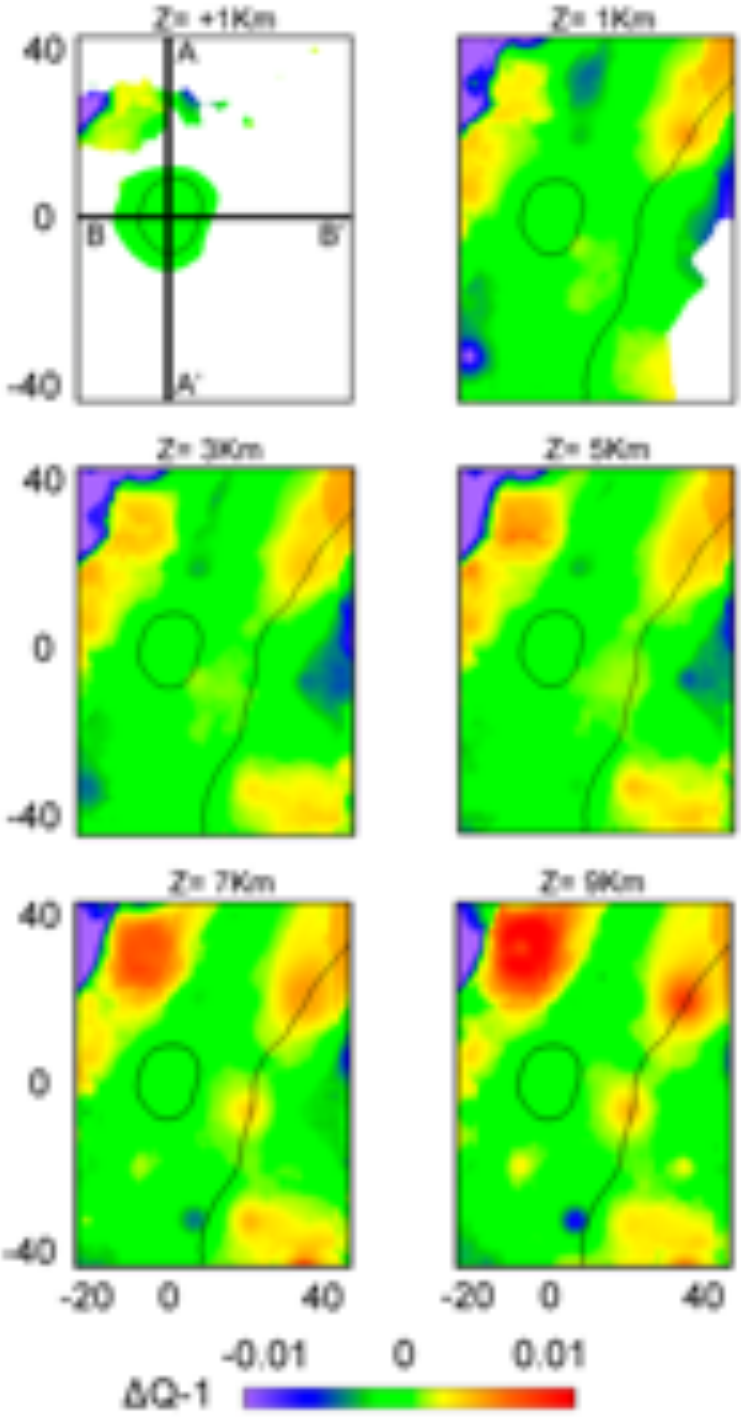

Figure 9

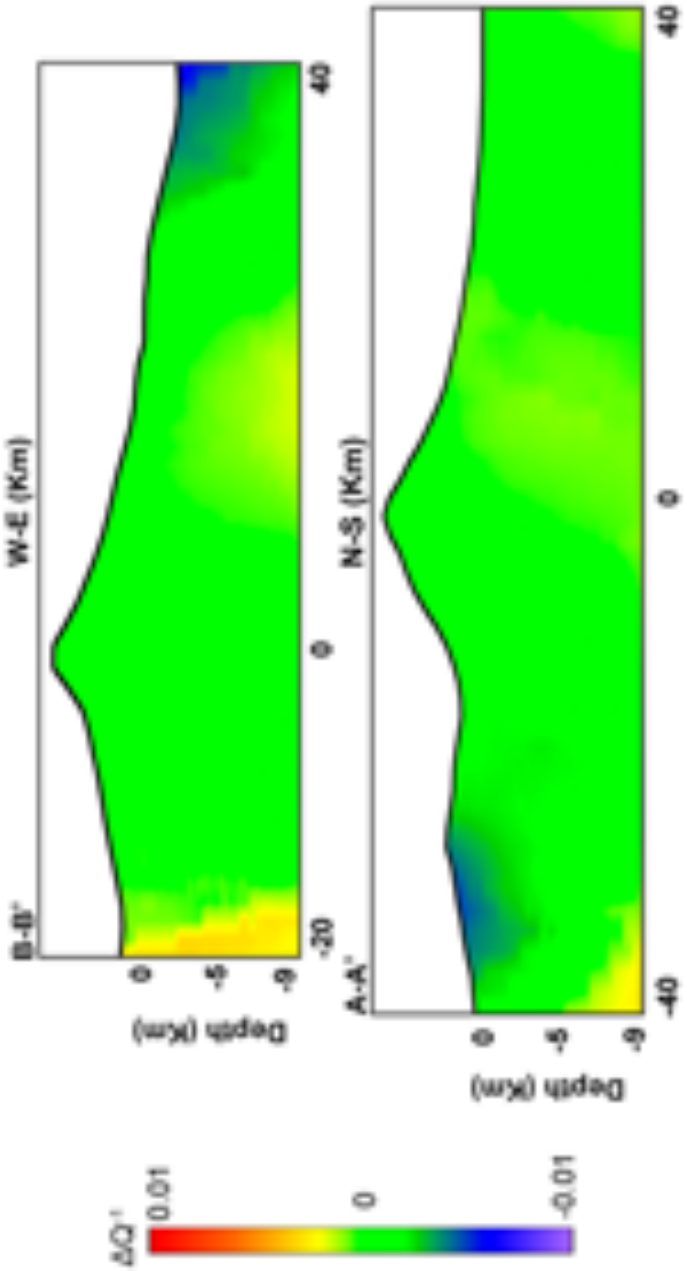
W-E (Km)
B-B'
40
0
-20
0
-5
-9
Depth (Km)
N-S (Km)
A-A'
40
0
-40
0
-5
-9
Depth (Km)
ΔQ⁻¹
0.01
0
-0.01

Figure 10

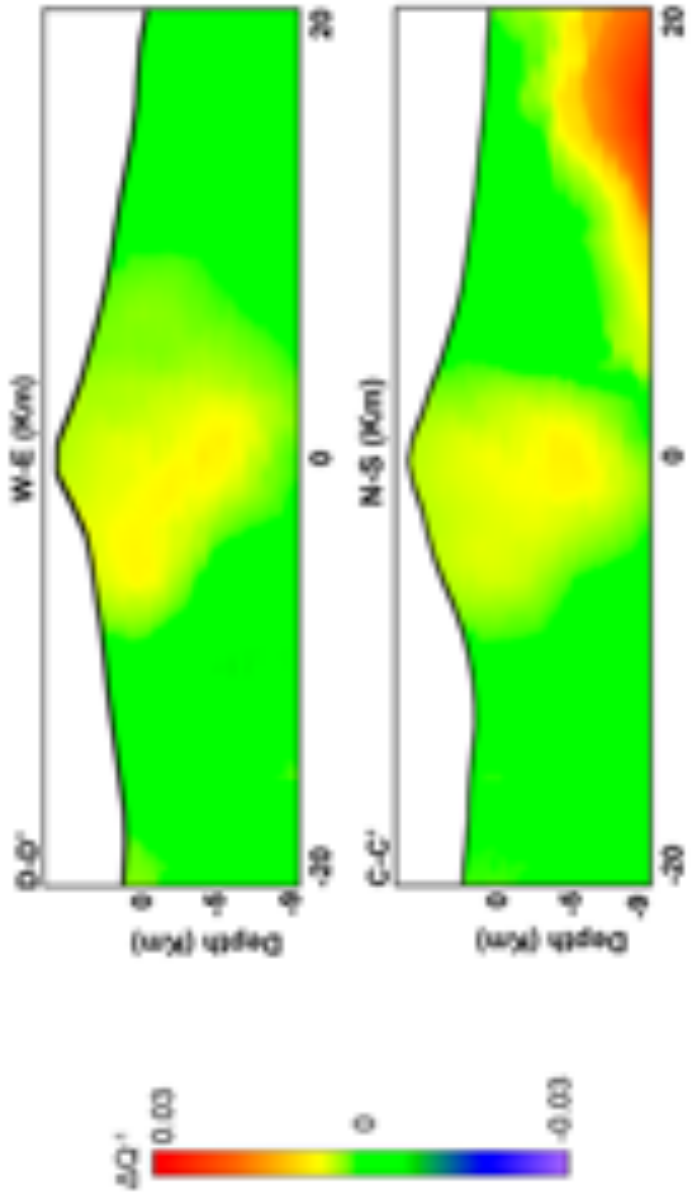
W-E (Km)
20
0
-20
D-D'
Depth (Km)
0
-8
-16
N-S (Km)
20
0
-20
C-C'
Depth (Km)
0
-8
-16
Δσ⁻¹
0.03
0
-0.03

Figure 11

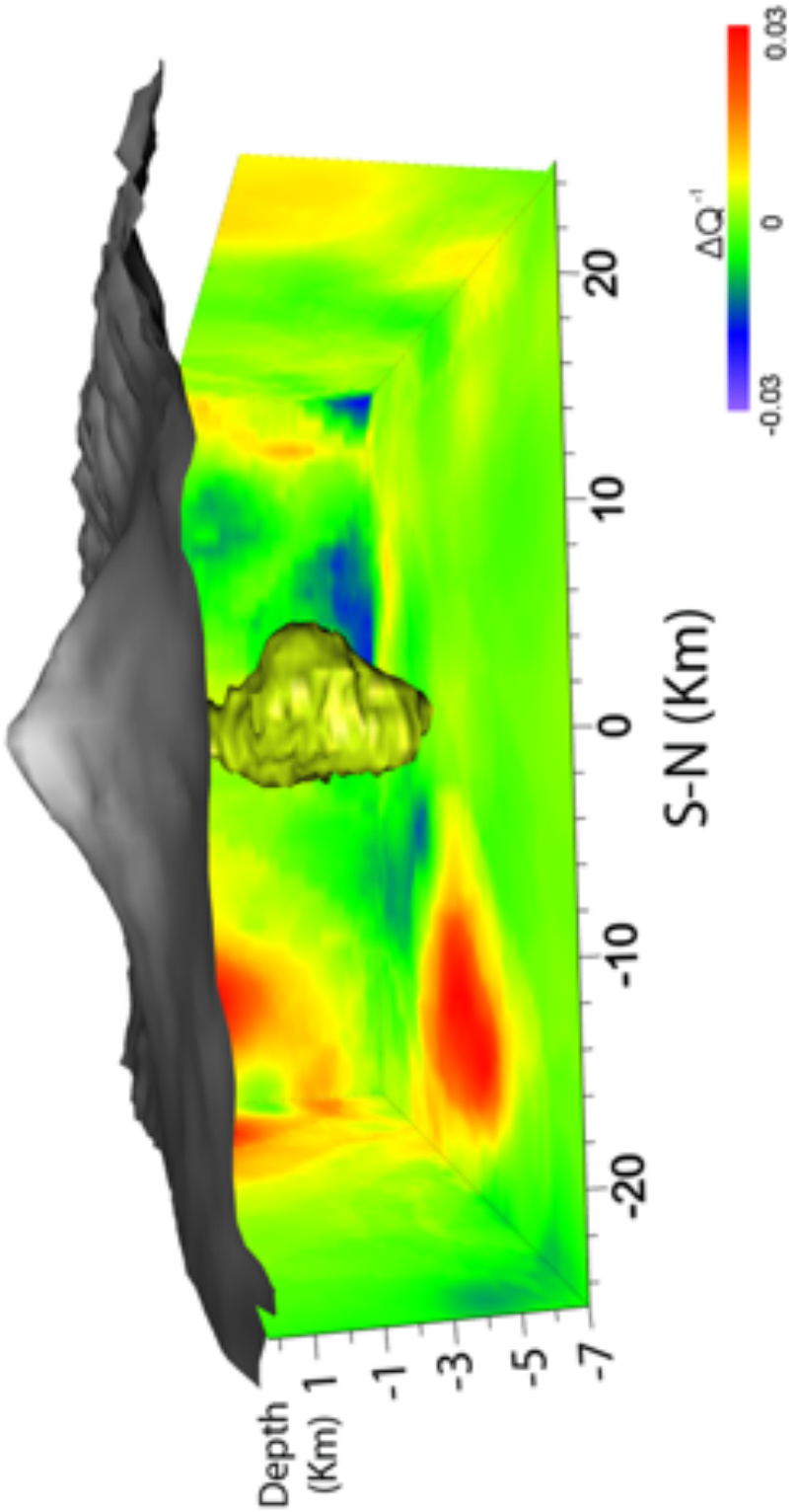
Depth (Km)
1
-1
-3
-5
-7
-20
-10
0
10
20
S-N (Km)
ΔQ⁻¹
0.03
0
-0.03

Figure 12.

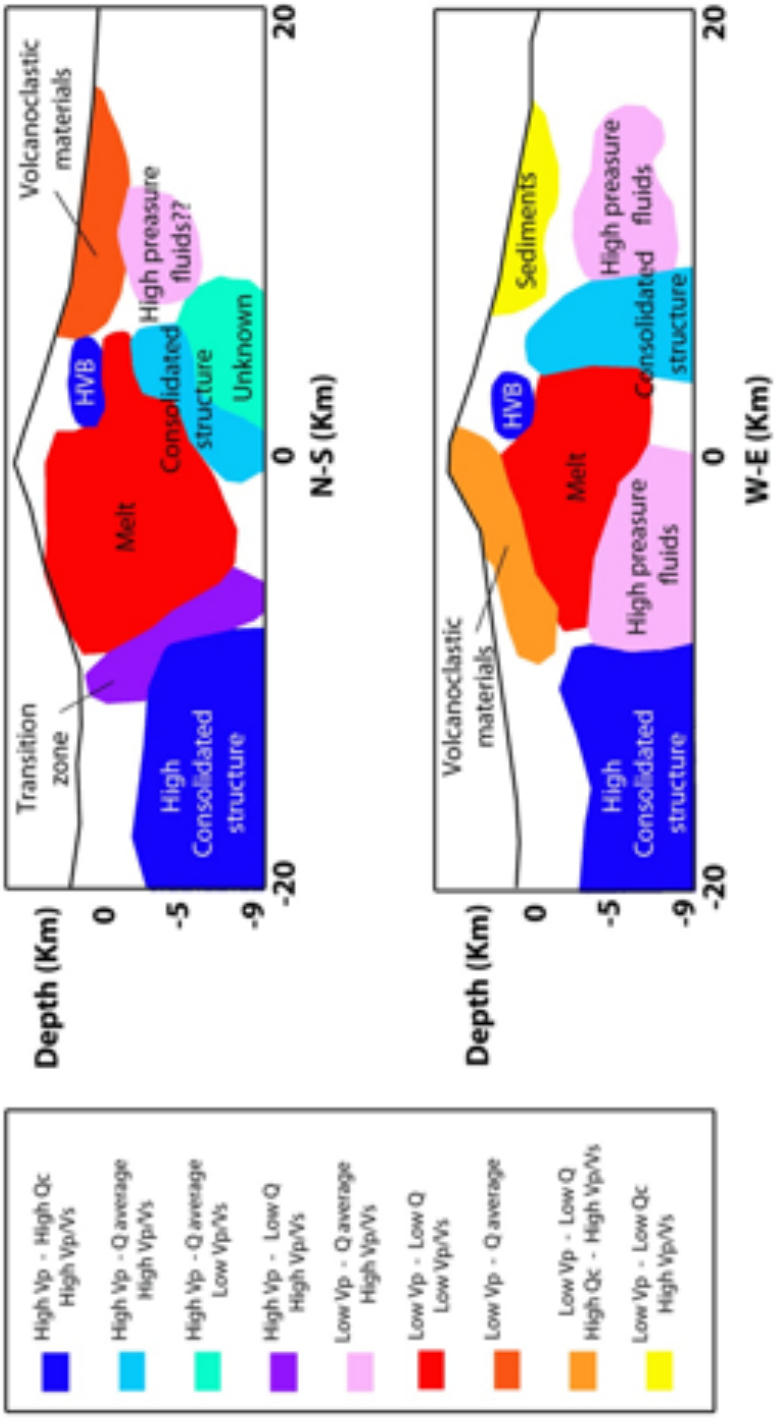
Depth (Km)
0
-5
-9
-20
0
20
N-S (Km)
Transition zone
Volcanoclastic materials
HVB
Melt
High Consolidated structure
Consolidated structure
High preasure fluids??
Unknown
W-E (Km)
Sediments
High preasure fluids
High preasure fluids
High Vp - High Qc
High Vp/Vs
High Vp - Q average
High Vp/Vs
High Vp - Q average
Low Vp/Vs
High Vp - Low Q
High Vp/Vs
Low Vp - Q average
High Vp/Vs
Low Vp - Low Q
Low Vp/Vs
Low Vp - Q average
Low Vp - Low Q
High Qc - High Vp/Vs
Low Vp - Low Qc
High Vp/Vs